

Stratospheric Age-of-Air: Sensitivity to Finite Volume Remapping Algorithm

Clara Orbe^{1,2}, Lawrence L. Takacs^{3,4}, Amal El Akkraoui^{3,4},
Krzysztof Wargan^{3,4}, Andrea Molod³, William Putman³, Steven Pawson³

¹NASA Goddard Institute for Space Studies, New York, NY

²Department of Applied Physics and Applied Mathematics, Columbia University, New York, NY

³Global Modeling and Assimilation Office, NASA Goddard Space Flight Center, Greenbelt, MD

⁴Science Systems and Applications, Inc., Lanham, MD, USA

Key Points:

- The stratospheric mean age-of-air simulated in GEOS is sensitive to the remapping scheme used within the finite-volume dynamical core.
- This sensitivity in the age-of-air is significant ($\sim 30\%$) and imprints on the simulated distributions of several long-lived chemical trace gases, including nitrous oxide and methane.
- The age-of-air sensitivities primarily reflect changes in resolved wave convergence over the Northern Hemisphere midlatitude stratosphere, which impact mean upwelling in the tropical lower stratosphere.

Corresponding author: Clara Orbe, clara.orbe@nasa.gov

18 **Abstract**

19 Accurately modeling the large-scale transport of trace gases and aerosols is critical for interpreting past (and projecting future) changes in atmospheric composition. 20 Simulations of the stratospheric mean age-of-air continue to show persistent biases in chemistry climate models, although the drivers of these biases are not well understood. Here 21 we identify one driver of simulated stratospheric transport differences among various NASA 22 Global Earth Observing System (GEOS) candidate model versions under consideration 23 for the upcoming GEOS Retrospective analysis for the 21st Century (GEOS-R21C). In 24 particular, we show that the simulated age-of-air values are sensitive to the so-called “remap- 25 ping” algorithm used within the finite-volume dynamical core, which controls how in- 26 dividual material surfaces are vertically interpolated back to standard pressure levels af- 27 ter each horizontal advection time step. Differences in the age-of-air resulting from changes 28 within the remapping algorithm approach ~ 1 year over the high latitude middle strato- 29 sphere - or about 30% climatological mean values - and imprint on several trace gases, 30 including methane (CH_4) and nitrous oxide (N_2O). These transport sensitivities reflect, 31 to first order, changes in the strength of tropical upwelling in the lower stratosphere (70- 32 100 hPa) which are driven by changes in resolved wave convergence over northern mid- 33 latitudes as (critical lines of) wave propagation shift in latitude. Our results strongly sup- 34 port continued examination of the role of numerics in contributing to transport biases 35 in composition modeling. 36 37

38 **Plain Language Summary**

39 Large-scale transport plays a crucial role in distributing climatically important trace 40 constituents in the atmosphere, especially in the stratosphere where transport largely 41 determines the chemical lifetimes of trace gases. One summary of transport in the strato- 42 sphere is the “mean age” or the mean transit time since air at a point in the stratosphere 43 was last in the troposphere. Current models used for simulating stratospheric compo- 44 sition produce a range of simulated ages, although these differences are poorly under- 45 stood. Among other factors, model numerics play a critical role in transport, but few 46 studies have explored the sensitivity of the mean age to the choice of numerical scheme 47 employed within different dynamical cores. Here we use one model to show that the mean 48 age is sensitive to the so-called “remapping” algorithm used within the finite-volume dy- 49 namical core that controls how individual material surfaces are vertically interpolated 50 back to standard pressure levels after each horizontal advection time step. This reflects 51 sensitivities in the representation of how waves propagate from the troposphere into the 52 stratosphere. This work suggests that model numerics can be an important factor in con- 53 tributing to differences in simulated transport among models.

54 **1 Introduction**

55 The chemical and radiative properties of the troposphere and lower stratosphere 56 are strongly influenced by the stratosphere-troposphere exchange of mass and tracers (e.g., 57 Morgenstern and Carver (2001); Hegglin et al. (2006); Pan et al. (2007)). Properly sim- 58 ulating the stratospheric circulation and its influence on atmospheric composition in earth 59 system models is important for capturing past decadal trends in surface climate, par- 60 ticularly in response to changes in Southern Hemisphere ozone depletion (e.g., Son et 61 al. (2009); Polvani et al. (2011)). In the Northern Hemisphere (NH), the stratospheric 62 circulation’s coupling to ozone could represent an important feedback on the climate’s 63 response to future increases in greenhouse gases (GHGs), especially over the North At- 64 lantic (e.g., Chiodo and Polvani (2019)). On shorter subseasonal timescales, stratospheric 65 ozone changes associated with strong polar vortex states may also modulate Arctic sea 66 level pressure and surface temperatures (e.g., Ivy et al. (2017); Oehrlein et al. (2020)), 67 so much so that seasonal forecast systems employing prognostic ozone show suggestions

68 of increased signal-to-noise ratio in predictions of the North Atlantic Oscillation (B. M. Monge-
69 Sanz et al. (2022)).

70 Key to accurately simulating a consistent representation of coupling between strato-
71 spheric dynamics and chemical trace gases is ensuring that a model’s underlying trans-
72 port circulation is properly represented. To this end, much effort has been paid to de-
73 veloping and refining so-called “tracer-independent” metrics of transport (Holzer and Hall
74 (2000)) such as the mean age-of-air (Hall and Plumb (1994)) and to applying these mea-
75 sures to rigorously evaluate model transport characteristics in chemistry climate mod-
76 els (CCMs) (e.g., Hall et al. (1999); Orbe et al. (2018); Dietmüller et al. (2018); Aba-
77 los et al. (2020)).

78 While the assessment of CCMs participating in the SPARC Chemistry Climate Model
79 Validation (SPARC CCMVal) effort showed a marked improvement in simulated trans-
80 port characteristics relative to previous intercomparisons (J. Neu et al. (2010)), more re-
81 cent analysis of models participating in the SPARC Chemistry Climate Modeling Ini-
82 tiative (CCMI) (Eyring et al. (2013)) do not demonstrate any improvement (Dietmüller
83 et al. (2018), see their Figure 3). In particular, although some models produce mean age
84 values that agree well with observational estimates, the CCMI intermodel spread is \sim
85 50%, with models generally simulating transport that is too vigorous relative to obser-
86 vations. While documenting these transport differences among models is straightforward,
87 understanding the drivers of this spread remains a key challenge and there is still no con-
88 sensus on what is causing the large spread in simulated ages among the current gener-
89 ation of CCMs.

90 A key challenge in identifying the drivers of age-of-air – and other stratospheric trans-
91 port – biases is that they reflect the time-integrated effects of advection by the residual
92 mean circulation and eddy diffusive mixing, or the quasi-random transport due to the
93 breaking of Rossby waves (e.g., Holton et al. (1995); Plumb (2002)). Given that the in-
94 fluences of mixing and advection are not easily separable, studies have come to differ-
95 ent conclusions about sources of age biases in models. In particular, the analysis of the
96 CCMVal models showed a strong correlation between the intermodel spread in the age-
97 of-air and lower stratospheric tropical upwelling, whereas Dietmüller et al. (2018) showed
98 that the age spread among the CCMI models was driven by differences in mixing. While
99 future attempts to further distinguish between sources of age biases using either simpli-
100 fied “leaky pipe” models (Plumb (1996); J. L. Neu and Plumb (1999)) or more complete
101 measures of the transport circulation such as the “age spectrum” (e.g., Hall and Plumb
102 (1994); Waugh and Hall (2002))) may prove enlightening, at present there is no consen-
103 sus on what is causing large simulated age-of-air biases in models.

104 One potential limitation of previous work based on multi-model intercomparisons
105 is that many aspects of model formulation can influence both stratospheric upwelling and
106 mixing. Thus, while intercomparisons are useful for identifying common model biases,
107 understanding the drivers of these biases is difficult absent single model-based process
108 studies. Among these, several aspects of model formulation have been identified as in-
109 fluencing simulated mean age distributions. As the mean age is sensitive to vertical mo-
110 tion in the lowermost stratosphere, these include large sensitivities to vertical resolution
111 (Orbe et al. (2020)) and to spurious vertical mixing either introduced in vertical coor-
112 dinate transformations in offline chemical transport models (B. Monge-Sanz et al. (2007))
113 or through use of assimilated winds performed either in offline (e.g., Legras et al. (2004))
114 or online data assimilation and “nudged” configurations (e.g., Pawson et al. (2007); Orbe
115 et al. (2017); Davis et al. (2022)). These age sensitivities can be still further amplified,
116 depending on whether or not parameterized gravity waves are included (Eichinger et al.
117 (2020)).

118 By comparison, sensitivities of the mean age to underlying tracer numerics have
119 been less well examined, although Eluszkiewicz et al. (2000) documented a large sensi-

120 tivity in simulated age-of-air values to the choice of advection scheme. More recently,
 121 Gupta et al. (2020) showed differences of $\sim 25\%$ in the age-of-air across identical exper-
 122 iments performed using four different dynamical cores, especially between those using
 123 spectral versus finite-volume schemes. The experiments employed in that study, how-
 124 ever, were highly idealized and it is not clear if the strong influence of tracer numerics
 125 that they identified is also realized in more comprehensive model simulations with moist
 126 physics, especially in the context of model development as carried out in operational mod-
 127 eling centers.

128 To better elucidate this influence of tracer numerics on the transport properties sim-
 129 ulated in a comprehensive global model context, here we document the sensitivity of the
 130 stratospheric mean age in several recent versions of the NASA Global Earth Observing
 131 System (GEOS) general circulation model (Molod et al., 2015) that represent different
 132 stages in model development since the Modern-Era Retrospective Analysis for Research
 133 and Applications Version 2 (MERRA-2; Gelaro et al. (2017)).

134 Our focus on transport evaluation is in wake of the upcoming release of the GEOS
 135 Retrospective analysis for the early 21st Century (GEOS-R21C), which will serve as an
 136 intermediate atmospheric reanalysis between MERRA-2 and the future coupled atmosphere-
 137 ocean reanalysis MERRA-3 (in-preparation). As part of the current effort to explore cou-
 138 pling of more Earth System components targeting MERRA-3, GEOS-R21C will be used
 139 to drive an off-line chemistry reanalysis R21C-Chem with a full chemistry model (GEOS-
 140 Chem) and an advanced Constituent Data Assimilation component to update the chem-
 141 istry fields. Since R21C-Chem will be produced in replay-mode (one-way coupling) whereby
 142 the meteorology fields are used to define the background atmospheric flow (Orbe et al.,
 143 2017), it is imperative that GEOS-R21C produces a credible representation of transport
 144 processes.

145 In particular, here we document how in the process of evaluating candidate sys-
 146 tems for GEOS-R21C we found that the mean age was ~ 1 year younger (or $\sim 30\%$ smaller)
 147 than the values simulated in the model version used to produce MERRA-2 (Figure 1).
 148 The model versions shown in Figure 1 reflect more than 10 years’ worth of accumulated
 149 changes in model development, most notably changes in radiation, parameterized con-
 150 vection and, as we focus on here, changes in the algorithm used to transform advected
 151 fields from Lagrangian levels to the new pressure levels after each horizontal advection
 152 time step. This is the model’s description of vertical advection. We show that slight mod-
 153 ifications in this so-called “remapping” algorithm are the primary driver of the age-of-
 154 air changes exhibited in recent GEOS-R21C candidate model versions, a result which
 155 may have broader implications for other general circulation models using finite volume
 156 (FV) dynamical cores. We begin by discussing methods in Section 2 and present key re-
 157 sults and conclusions in Sections 3 and 4, respectively.

158 2 Methods

159 2.1 Model Configurations

160 Here we present results from several versions of GEOS spanning MERRA-2 to more
 161 recent candidates for GEOS-R21C. Among these model versions, a subset are more “of-
 162 ficial” as they have been documented and/or employed in recent model intercomparisons
 163 and are highlighted in Figure 1. In particular, these include a model version that was
 164 used in Phase 1 of CCM1 and documented in Orbe et al. (2017) (Fig. 1, red line). A more
 165 recent model version that was used in the CCM1 Phase 2 simulations (correspondence
 166 with Michael Manyin) is also shown (Fig. 1, green line).

167 We begin by comparing 10-year (2000-2010) climatological mean zonally averaged
 168 age-of-air profiles at 50 hPa across this subset of model versions, derived from 30-year
 169 long atmosphere-only (AMIP) integrations constrained with observed sea surface tem-

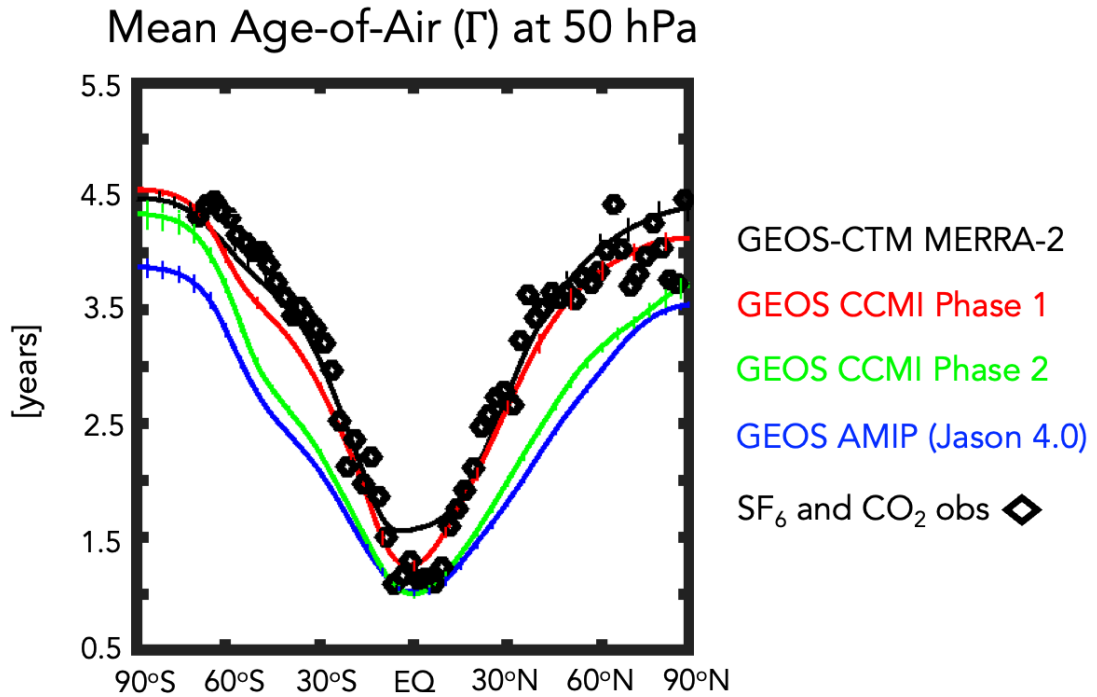


Figure 1. The 2000-2010 climatological annual mean meridional profile of the stratospheric mean age-of-air (Γ), evaluated at 50 hPa. Results from a GEOS-CTM integration constrained with MERRA-2 meteorological fields (black line) as well as free-running GEOS simulations using a model configuration for CCM1 Phase 1 (red line), CCM1 Phase 2 (green line) and a more recent GEOS-FP development tag (Jason 4.0, blue line) are shown. All simulations are constrained with the same (observed) historical sea surface temperatures. Diamonds correspond to SF₆ and CO₂ in situ based estimates of Γ from Boering et al. (1996) and Engel et al. (2009). Vertical dashed lines denote $\pm\sigma$, the standard deviation of Γ over 2000-2010, for each model simulation.

170 peratures (Figure 1). First, we note that the profiles for the CCMI Phase 1 version of
 171 the model are very close to observations (black stars), consistent with the
 172 “GEOSCCM” documented age characteristics reported in Dietmüller et al. (2018) (see
 173 their Figure 3). In addition, while passive tracers were not integrated within MERRA-
 174 2, results using the GEOS chemistry transport model (GEOS-CTM, Kouatchou et al.
 175 (2015)) constrained with MERRA-2 meteorological fields (black line) also exhibits good
 176 agreement with observed values. This good agreement between the CTM-generated age-
 177 of-air and the observations is consistent with results from a previous GEOS-CTM sim-
 178 ulation (constrained with MERRA) as documented in Orbe et al. (2017).

179 Moving to more recent development versions of the model (green and blue lines),
 180 however, reveals a reduction in the mean age by ~ 1 year over both southern and north-
 181 ern high extratropical latitudes, or a decrease of ~ 20 -30% relative to the MERRA-2 con-
 182 strained simulation and the observations. As discussed earlier, the green line refers to
 183 the CCMI Phase 2 model version, whereas the blue line refers to an undocumented can-
 184 didate version (model tag Jason 4.0) that corresponds best to a model configuration sim-
 185 ilar to what is used in the GEOS forward processing (FP) numerical weather prediction
 186 system. Note that this decrease in the climatological age in both model versions far ex-
 187 ceeds the (internal) variations in mean age that occur interannually (vertical bars on solid
 188 lines).

189 There are numerous development updates in the model that have occurred since
 190 MERRA-2. Therefore, after discussing the model configurations highlighted in Figure
 191 1 in Section 3.1, we then present results from targeted experiments aimed at successively
 192 undoing these changes one-by-one (Section 3.2). Among those aspects most relevant to
 193 the stratospheric transport circulation, we first present results from experiments which
 194 undo recent changes in the radiation scheme, which was updated from Chou and Suarez
 195 (1994) in the shortwave and Chou (1990, 1992) in the longwave to the Rapid Radiative
 196 Transfer Model for GCMS (RRTMG; Iacono et al. (2008).

197 XI

198 After addressing the radiation changes, we focus on a still more consequential up-
 199 date that was made to the handling of the remapping algorithm within the model’s FV
 200 dynamical core (Lin, 2004). Within the FV core vertical motion is realized through the
 201 Lagrangian transport of the “floating” vertical coordinate such that after each horizon-
 202 tal advection step the individual material surfaces are vertically interpolated back to the
 203 model’s reference Eulerian coordinate through FV’s so-called “REMAP” algorithm. This
 204 is needed because the Lagrangian surfaces that vertically bound the finite volumes will
 205 eventually deform, negatively impacting the accuracy of the horizontal-to-Lagrangian-
 206 surface transport and the computation of the pressure-gradient terms.

207 Since MERRA-2 several changes were made to the remapping algorithm. In its cur-
 208 rent implementation the algorithm involves 1) fitting piecewise parabolic (hereafter PPM)
 209 functions to input layer-mean values of T, U, V, Q and tracers; 2) calculating PPM func-
 210 tions to output layer edges; and 3) integrating PPM functions between output layer edges
 211 to produce new layer-mean values of T, U, V, Q and tracers. Note that T, U, V, Q, C_p ,
 212 K and Φ correspond to temperature, zonal wind, meridional wind, specific humidity, spe-
 213 cific heat capacity and kinetic and potential energy, respectively. This implementation
 214 is consistent with what is currently being used in most recent GEOS model versions (i.e.
 215 blue and green lines, Figure 1) and hereafter is referred to as REMAP Option 2 (Table
 216 1, left).

217 The alternative version – which best mimics what was used in MERRA-2 – involves
 218 two main changes to this procedure and is hereafter referred to as REMAP Option 1 (Ta-
 219 ble 1, right; red line in Figure 1). First steps 1) and 3) are performed only for U, V, Q
 220 and tracers (not T). Second, three additional steps after 3) are added, the first two of

Table 1. Finite Volume Remapping Algorithm: The two versions examined in this study control how individual material surfaces are vertically interpolated back to standard pressure levels. REMAP Options 2 and 1 corresponds to the configurations used in more recent (green and blue lines, Figure 1) and older (red and black lines, Figure 1) model configurations, respectively. Here T, U, V, Q, C_p , K and Φ correspond to temperature, zonal wind, meridional wind, specific humidity, specific heat of air at constant pressure and kinetic and potential energy, respectively.

Step	REMAP Option 2 (CTRL)	REMAP Option 1 (MERRA-2)
1	Fit PPM functions to input layer-mean T, U, V, Q and tracers	Fit PPM functions to input layer-mean U, V, Q and tracers
2	Calculate PPM to output layer edges	Calculate PPM to output layer edges
3	Integrate PPM functions between output layer edges to produce new layer-mean T, U, V, Q and tracers	Integrate PPM functions between output layer edges to produce new layer-mean U, V, Q and tracers
4	n/a	Calculate TE = $C_p T + K + \Phi$ at input mid-layer pressures
5	n/a	Calculate TE at output mid-layer pressures using cubic interpolation and a-posteriori integral conservation
6	n/a	Construct “remapped” T via $T = (TE - K - \Phi)/C_p$

221 which involve calculating total energy (TE) at input mid-layer pressures and then per-
 222 forming cubic interpolation and a posteriori integral conservation at output mid-layer
 223 pressures. Finally, temperatures are “remapped” from total energy via $T = (TE - K -$
 224 $\Phi)/C_p$.

225 When examining Table 1, it is important to note that Options 1 and 2 differ in two
 226 main respects. The most consequential difference involves the interpolation that occurs
 227 within step 5 in REMAP Option 1. By comparison, the use of TE (as opposed to T),
 228 is less consequential and has no major impact on the circulation (Appendix Figure A1a).
 229 To this end, the sensitivity experiments discussed in the next section mainly focus on
 230 identifying the age-of-air sensitivities to changes in the interpolation scheme used in REMAP
 231 Option 1, not to the change from the use of TE to T.

232 Finally, it is worth noting other important model development changes that occurred,
 233 particularly those related to the parameterization of deep convection (Grell and Freitas
 234 (2014); Freitas et al. (2018)), could directly impact the stratospheric circulation by in-
 235 fluencing wave generation in the troposphere. Although these changes have had a sub-
 236 stantial impact on the diurnal cycle of precipitation (Arnold et al. (2020)) and on con-
 237 vective transport within the troposphere (Freitas et al. (2020)), their influence on the
 238 large-scale stratospheric circulation is much smaller relative to the remapping and ra-
 239 diation changes.

240 2.2 Model Experiments

241 2.2.1 AMIP vs. EMIP

242 We begin our analysis by interpreting the results shown in Figure 1, which are all
 243 based on historical AMIPs that were performed at the same cubed sphere C180 (approx-
 244 imately half-degree) horizontal resolution. As they represent more official model versions

245 they serve as an important motivation for the experiments that follow. However, there
 246 are numerous (potentially compensating) development changes between these model ver-
 247 sions which renders it nearly impossible to cleanly identify drivers of differences in their
 248 simulated transport.

249 To this end, in order to investigate the drivers of the differences in Figure 1 we per-
 250 form targeted modeling experiments aimed at disentangling the influence of individual
 251 model development changes on stratospheric transport properties (Table 2). In order to
 252 evaluate impacts on transport climate statistics, we consider both a set of climatolog-
 253 ical AMIP (rows 1-4) as well as so-called “EMIP” (rows 5-7) experiments.

254 In particular, we carry out 30-year-long AMIP simulations at C180 resolution which
 255 we use to infer the climate characteristics of the different model configurations. The “EMIP”
 256 experiments – ensembles of 3-month-long integrations initialized on approximately Novem-
 257 ber 15 of each year between 1985 and 2015 – are also used to infer impacts on simulated
 258 transport climate. As they are more computationally efficient than AMIPs since all 30
 259 3-month integrations may be run in parallel, they are performed at both C180 and C360
 260 resolutions in order to examine the sensitivity of our results to changes in horizontal res-
 261 olution.

262 As shown in Appendix B, comparisons of the December-January-February (DJF)
 263 vertical profile of tropical upwelling show excellent agreement between EMIP and AMIP
 264 integrations carried out using the same model configuration (Appendix Figure B1). This
 265 somewhat incidental result represents, to the best of our knowledge, the first time that
 266 EMIP-based statistics have been shown to converge well to those from AMIPs for the
 267 stratospheric metrics considered in this study. This suggests that EMIPs, relative to AMIPs,
 268 may be used to provide a computationally more efficient initial assessment of the impacts
 269 of model changes on the stratospheric circulation.

270 **2.2.2 Model Development Changes**

271 Moving next to the precise model development changes examined, we begin by defin-
 272 ing a control experiment (CTRL; Table 2, row 1), which best corresponds to the blue
 273 line shown in Figure 1. Then we define three new AMIP experiments, each based on this
 274 control, that are used to distinguish between the age-of-air changes resulting from changes
 275 in radiation versus changes in the handling of the REMAP algorithm (Section 3.2.1).

276 Specifically, these include experiments in which we a) revert back from RRTMG
 277 to the radiation from Chou and Suarez (1994) (CSRAD; Table 2, row 2), b) revert back
 278 to the MERRA-2 REMAP approach (i.e. REMAP Option 1) (M2REMAP; Table 2, row
 279 3) and c) combine these two changes (CSRAD+M2REMAP; Table 2, row 4).

280 As we show in Section 3.2.1, the M2REMAP experiment produces the largest changes
 281 in age-of-air, compared to the experiment in which only the radiation is altered. To this
 282 end, we focus the remainder of our investigation (Section 3.2.2) on examining a clean
 283 set of EMIP experiments run at both C180 and C360 horizontal resolutions that distin-
 284 guish the impact of REMAP Option 1 versus Option 2 on simulated transport. In par-
 285 ticular, we perform three sensitivity experiments that differ from each other only in terms
 286 of the calculation of TE at the mid-layer pressure levels, which we perform using a lin-
 287 ear (LINEAR; Table 2, row 5), quadratic (QUADRATIC; Table 2, row 6) and cubic in-
 288 terpolation (CUBIC; Table 2, row 7) scheme, with the latter corresponding to the ap-
 289 proach that was used in MERRA-2.

290 These three numerical schemes are derived from the generic interpolation equation:

$$Q(\mathcal{P}) = \sum_{k'} a_{k+k'} Q_{k+k'} \quad k' = 0, \pm 1, \pm 2, \dots \quad (1)$$

Table 2. GEOS Model Experiments: Targeted GEOS model experiments based off a control experiment (row 1) were carried out to identify the influence of radiation (row 2) and the FV remapping algorithm changes since MERRA-2 (row 3), as well as their combined influence (row 4). Sensitivities within the FV remapping algorithm were further explored with respect to the order of the interpolation scheme used to calculate TE at output mid-layer pressure levels (rows 5-7). Experiments in rows 1-4 are 30-year-long AMIPs run at C180 resolution, whereas rows 5-7 refer to 30-member 3-month-long (DJF) EMIP experiments. Both AMIPs and EMIPs are used for climate statistic evaluation (see Appendix A for more on the correspondence between the two). EMIP experiments are run at both C180 and C360 horizontal resolutions.

Experiment Name	Configuration	Experiment Type	Hor. Resolution
CTRL	Control, REMAP Option 2	AMIP (30 yrs.)	C180
CSRAD	Chou-Suarez (1994) Radiation (RAD)	AMIP (30 yrs.)	C180
M2REMAP	MERRA-2 REMAP Option 1 (cubic)	AMIP (30 yrs.)	C180
CSRAD+M2REMAP	Chou-Suarez (1994) RAD REMAP Option 1 (cubic)	AMIP (30 yrs.)	C180
LINEAR	MERRA-2 REMAP Option 1 (linear)	EMIP (30 mem.)	C180, C360
QUADRATIC	MERRA-2 REMAP Option 1 (quadratic)	EMIP (30 mem)	C180, C360
CUBIC	MERRA-2 REMAP Option 1 (cubic)	EMIP (30 mem)	C180, C360

291 where \mathcal{P} represents the target output location in $\ln(p)$ and $\mathcal{Q}_{k+k'}$ denotes the surround-
 292 ing grid-point values at input locations. The coefficients $a_{k+k'}$ are derived through Tay-
 293 lor Series expansions using non-uniform grid spacing given by:

$$a_{k+k'} = \frac{\Pi_m (\mathcal{P}_{k+m} - \mathcal{P})}{\Pi_m (\mathcal{P}_{k+m} - \mathcal{P}_{k+k'})} \quad m = 0, \pm 1, \pm 2, \dots \quad m \neq k' \quad (2)$$

294 For the three schemes, the grid points used are: LINEAR ($k, k-1$), QUADRATIC ($k+$
 295 $1, k, k-1$), and CUBIC ($k+1, k, k-1, k-2$). In all cases, the grid points are chosen
 296 such that the target location resides between layers k and $k-1$.

297 Note that, while the LINEAR and QUADRATIC experiments do not actually cor-
 298 respond to any of the model versions shown in Figure 1, they highlight the large sensi-
 299 tivity of the mean age to changes in the interpolation scheme that may otherwise seem
 300 innocuous. They also provide further evidence of the strong influence of changes in trop-
 301 ical lower stratospheric upwelling strength on the stratospheric mean age in GEOS.

302 Finally, in all experiments using REMAP Option 1 (i.e. M2REMAP, CSRAD+
 303 M2REMAP, LINEAR, QUADRATIC, CUBIC) additional modifications to the diver-
 304 gence damping coefficients were used so as to best ensure consistency with what was used
 305 in MERRA-2. Specifically, these include changes to the number of layers for vertical sub-
 306 grid mixing, the coefficient for barotropic mode damping, the use of 2nd vs. 6th order
 307 divergence damping and the strength of the divergence damping coefficients.

308 2.3 Analysis Approach

309 2.3.1 Transport Diagnostics

310 To diagnose the transport circulation we focus primarily on the age-of-air (Hall and
 311 Plumb (1994)). This is inferred from an idealized global “clock” or ideal age tracer (Γ)
 312 (Thiele and Sarmiento (1990)) that is defined with respect to the bottom model level
 313 as follows: initially, the ideal age tracer is set to zero throughout the troposphere and
 314 thereafter held to zero over the entire Earth’s surface, subject to a constant aging of 1
 315 year/year throughout the atmosphere. We present here the statistically stationary (equi-
 316 librated) value of $\Gamma(r)$, which is equal to the average time since the air at a location r
 317 in the stratosphere last contacted the Earth’s surface. In addition to the mean age, we
 318 also show results from an idealized e90 tracer that is uniformly emitted over the entire
 319 surface layer and decays exponentially at a rate of 90 days⁻¹ such that concentrations
 320 greater than 125 ppb and less than 50 ppb tend to reside in the lower troposphere and
 321 stratosphere, respectively (Prather et al. (2011)). As this tracer features strong near-
 322 tropopause gradients and takes significantly less time to equilibrate, compared to the mean
 323 age, it is useful for evaluating stratosphere-troposphere-exchange and transport within
 324 the upper troposphere/lower stratosphere (Abalos et al. (2017, 2020); Orbe et al. (2020)).

325 Both the mean age and e90 tracers were integrated in all of the AMIP experiments
 326 shown in Figure 1 and listed in Table 2 (rows 1-4), which were run using the same ide-
 327 alized passive tracer package described in Orbe et al. (2017). Note that the mean age
 328 tracer was not integrated in the EMIP experiments given its much longer characteris-
 329 tic timescale in the stratosphere (~ 3 -5 years). As such, the EMIP simulations, which
 330 do not exceed one year, are not appropriate for evaluating the time-integrated transport
 331 characteristics reflected in the age-of-air.

332 In addition to carrying the idealized tracers, two of the experiments shown in Fig-
 333 ure 1 were also run with full interactive chemistry and correspond to the two CCM1 (Phase
 334 1 and Phase 2) integrations (red and green lines, Figure 1). Both simulations employ the
 335 same Global Modeling Initiative (GMI) chemical mechanism (Strahan et al. (2013)) and
 336 are therefore useful in evaluating the impact of age differences on real trace gas distri-

337 butions. In particular, as shown in Section 3.1 results from these experiments show sig-
 338 nificant imprints of the age-of-air changes on nitrous oxide (N_2O) and methane (CH_4).

339 2.3.2 Circulation Diagnostics

340 As we show in Section 3, the changes in age-of-air across the different model ver-
 341 sions are strongly tethered to changes in the advective component of the circulation, which
 342 we quantify using the Transformed Eulerian Mean (TEM) estimate of the Lagrangian
 343 transport of mass by the circulation. Thus, in addition to more standard Eulerian met-
 344 rics of the circulation (e.g., zonal winds and temperatures), we focus on the vertical com-
 345 ponent of the TEM residual velocity, defined as $\bar{w}^* = \bar{w} + \frac{\partial(\psi \cos\phi)}{\text{acos}\phi\partial\phi}$, where $\psi = \overline{v'\theta'}/\frac{\partial\theta}{\partial p}$
 346 is the eddy stream function, θ refers to potential temperature, a is the Earth's radius
 347 and overbars and primes denote zonal means and deviations therefrom, respectively (Andrews
 348 et al. (1987)). In addition, we interpret the behavior in w^* using the Eliassen-Palm flux
 349 divergence ($\nabla \cdot \mathbf{F}$), whose horizontal ($\mathbf{F}(\phi)$) and vertical ($\mathbf{F}(p)$) components are respec-
 350 tively defined as $\mathbf{F}(\phi) = \text{acos}\phi[\frac{\partial u}{\partial p}\psi - \overline{u'v'}]$ and $\mathbf{F}(p) = \text{acos}\phi([\mathbf{f} - \frac{\partial u \cos\phi}{\text{acos}\phi\partial\phi}]\psi - \overline{u'\omega'})$.

351 2.4 Observations and Reanalyses

352 While our focus is on interpreting and understanding the different model config-
 353 urations, we incorporate observations to provide context when possible, although we do
 354 not present an exhaustive evaluation of the model's transport characteristics (for that
 355 see earlier studies including Orbe et al. (2017, 2018)). However, as the tracers are not
 356 directly integrated in MERRA-2 (with the exception of ozone), we compare against in-
 357 dependent observational estimates. For the mean age we first compare simulated merid-
 358 ional age profiles at 50 hPa with values derived from in situ aircraft measurements of car-
 359 bon dioxide (CO_2), averaged in 2.5 degree latitude bins over the altitude range 19.5 to
 360 21.5 km (Boering et al. (1996), see also Figure 5 in Hall et al. (1999)).

361 We also briefly evaluate impacts of transport biases on the simulated trace gas dis-
 362 tributions for the CCM1 Phase 1 and 2 experiments. The simulated fields of methane
 363 (CH_4) are compared with the climatologies derived for 1991–2002 from the Halogen Oc-
 364 cultation Experiment (HALOE) on board the Upper Atmosphere Research Satellite (UARS)
 365 (Grooß and Russell III (2005)). Comparisons of simulated nitrous oxide (N_2O) are made
 366 against climatologies derived from the Microwave Limb Sounder (MLS) on the Earth Ob-
 367 serving System (EOS) Aura satellite. Climatologies over the same period (2005–2015)
 368 are used to evaluate both the model and the observations. We use the 190-GHz retrieval
 369 from Version 4.2 because the 640-GHz data set ends in summer 2013 due to the failure
 370 of the N_2O primary band.

371 For the circulation diagnostics nearly all comparisons are made relative to the MERRA-
 372 2 data assimilation (DAS) reanalysis product, noting that comparisons against ERA-5
 373 (not shown) reveal a similar picture. One exception, however, is the vertical component
 374 of the TEM circulation (w^*), which shows some differences in vertical structure between
 375 MERRA-2 and a 30-member ensemble of (free-running) AMIP integrations produced us-
 376 ing the MERRA-2 model, hereafter referred to as M2AMIP (Collow et al., 2017)(Ap-
 377 pendix Figure A1, right). As the free-running model results shown in Figure 1 show more
 378 consistency with the vertical profile of M2AMIP, not MERRA-2, we compare w^* in all
 379 free-running GEOS experiments with M2AMIP, noting that for non-derived measures
 380 (i.e., winds, temperatures), the raw MERRA-2 output is used.

381 The differences in w^* between M2AMIP and MERRA-2 may reflect the influence
 382 of temperature increments in the DAS (MERRA-2) which can drive spurious vertical trans-
 383 port in assimilated products (Weaver et al., 1993; Orbe et al., 2017). In particular, Weaver
 384 et al. (1993) showed that the imbalance between the thermal and velocity fields at the
 385 time an observation is ingested during the assimilation cycle can excite unwanted inertial-

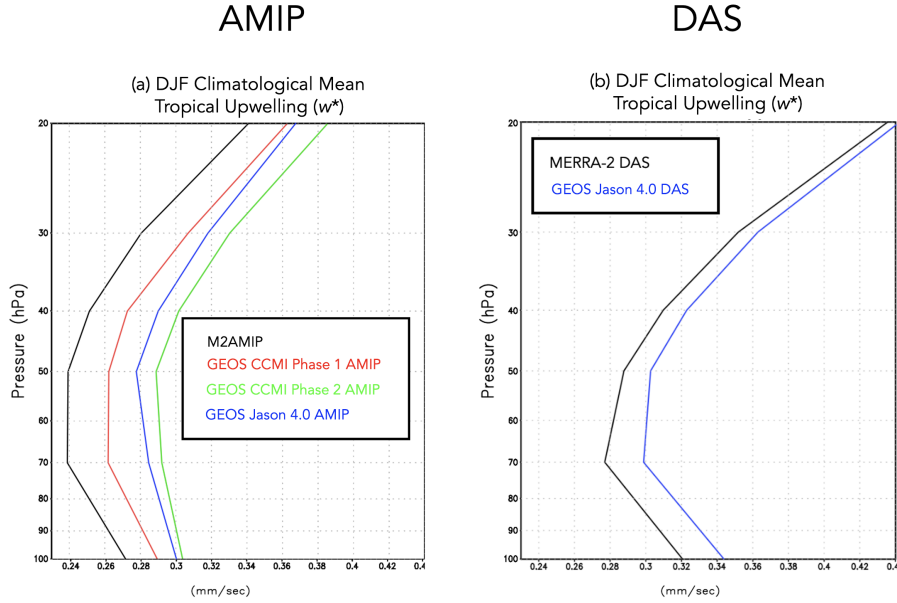


Figure 2. Left: The DJF climatological mean vertical residual mean velocity, w^* , averaged between the turnaround latitudes for GEOS free-running AMIP simulations using the model configurations corresponding to the CCM1 Phase 1 (red) and Phase 2 (green) submissions and to Jason 4.0 (blue). M2AMIP is shown in black. Right: The DJF climatological mean vertical residual mean velocity, w^* , averaged between the turnaround latitudes for MERRA-2 (black) and a data-assimilation configuration of Jason 4.0 (blue). Note that the right panel only uses limited data from years 1997-2021 for which the Jason 4.0 DAS output was available. As they reflect more recent years, the MERRA-2 DAS values in the right panel are therefore larger than the values shown in Figure A1b, given that w^* has increased over more recent decades (see Figure 5.14 in (Fujiwara et al., 2022)).

386 gravity wave modes that manifest strongly in the residual vertical winds. This impact
 387 of the increments may therefore explain the differences in w^* , particularly above 30 hPa,
 388 where the contribution of temperature increments to the analysis is large. We empha-
 389 size, however, that our main interest in this study is on upwelling within the lower strato-
 390 sphere (i.e., 70-100 hPa), where M2AMIP and MERRA-2 agree well, as this region best
 391 correlates with the global age-of-air characteristics. As such, we reserve further explo-
 392 ration of the w^* differences above 50 hPa for future work.

393 3 Results

394 3.1 Reduction of Stratospheric Mean Age in GEOS Models 395 Since MERRA-2

396 We begin by interpreting the reduction in mean age exhibited in more recent model
 397 versions in terms of changes in the strength of upwelling in the tropical lower stratosphere.
 398 In particular, the reductions in Γ (Figure 1) are consistent with increases in the strength
 399 of lower stratospheric tropical upwelling, with w^* becoming progressively stronger in more
 400 recent model versions, relative to MERRA-2 (Figure 2a). Note that, while the increases
 401 in w^* occur throughout the stratosphere, we focus on the changes occurring between 70
 402 and 100 hPa as these are most relevant to determining the tropical upward mass flux and
 403 associated strength of the mean overturning circulation.

404 Interestingly, the increases in w^* relative to MERRA-2 are not only manifest in 30-
 405 year-long AMIPs (Fig. 2a), but also in a DAS configuration of the Jason 4.0 model tag
 406 (Fig. 2b), evaluated over a more recent period spanning 1997 to 2021. Though not the
 407 main focus of this study, this impact on the DAS simulations has important implications
 408 for the development of R21C as it highlights that the assimilation of observations may
 409 reduce, but not entirely correct for, the model transport biases that have been introduced
 410 in more recent GEOS model versions.

411 Though perhaps naive, the relationship between lower stratospheric upwelling and
 412 the mean age suggested by comparing Figure 1 and Figure 2a is consistent with the long-
 413 term behavior of Γ inferred from both historical and projected future climate simulations
 414 (Butchart et al. (2010); Abalos et al. (2021)). A strong relationship between the strength
 415 of lower stratospheric ascent and the mean age was also shown to hold in the CCMVal
 416 models (see Fig. 5.20 in J. Neu et al. (2010)). Nevertheless, it is important to note that
 417 a clear relationship between w^* and Γ is not a priori expected, as the age-of-air is also
 418 known to be very sensitive to mixing, which may be important in interpreting differences
 419 among the CCMI Phase 1 models (Dietmüller et al. (2018)).

420 The differences in w^* highlighted in Figure 2 are associated with enhanced Eliassen-
 421 Palm flux convergence over NH midlatitudes (Figure 3). Increased wave convergence is
 422 evident not only within the subtropical lower stratosphere ($< 30^\circ\text{N}$, 50-100 hPa) but also
 423 over higher latitudes and altitudes ($\sim 40^\circ\text{-}70^\circ\text{N}$, 20-50 hPa). The fact that differences
 424 in extratropical wave convergence imprint on tropical upwelling is consistent with our
 425 understanding of the so-called “downward control” principle (Haynes et al. (1991)).

426 In particular, the strength of the residual mean streamfunction (Ψ^*) is, via down-
 427 ward control, directly related to the vertically integrated eddy-induced total zonal force
 428 above that level and has contributions both from the (resolved wave) Eliassen-Palm flux
 429 divergence (Figure 3) as well as the gravity wave drag scheme’s parameterized waves (not
 430 shown). The tropical upward mass flux – defined as $\Psi_{\text{max}}^* - \Psi_{\text{min}}^*$ evaluated at the turnaround
 431 latitudes (e.g. Rosenlof (1995)) – is therefore directly dependent on the wave forcing aloft.

432 One subtlety to note is that the wave convergence changes shown in Figure 3 oc-
 433 cur at high latitudes and are directly associated with downwelling over the polar region.
 434 It is then via mass balance that anomalously strong downwelling associated with enhanced

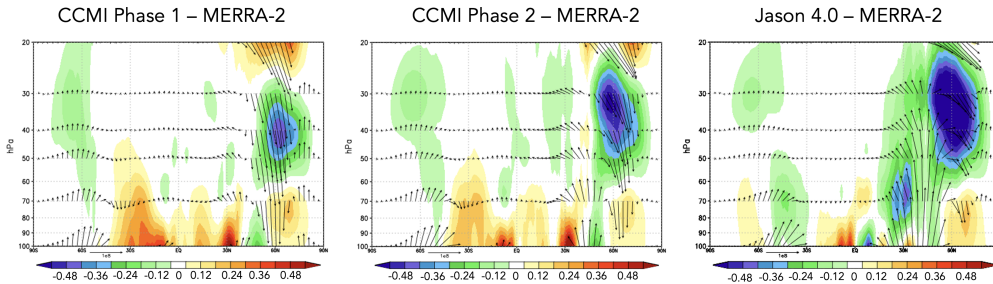
DJF Climatological Mean Eliassen-Palm Flux Divergence ($\nabla \cdot \mathbf{F}$)

Figure 3. Colors show anomalies in the DJF climatological mean Eliassen-Palm (EP) flux divergence between the CCMI Phase 1 (left), CCMI Phase 2 (middle) and Jason 4.0 GEOS AMIP (right) model versions, relative to MERRA-2. Arrows denote anomalies in the vertical and meridional EP flux vectors (relative to MERRA-2).

435 flux convergences must be accompanied by enhanced upwelling in the tropics. This in-
 436 direct impact of higher latitude wave drag reflects an “extratropical pumping” mecha-
 437 nism (Holton et al., 1995), which is illustrated more clearly in Section 3.2.2 in the con-
 438 text of the LINEAR, QUADRATIC and CUBIC experiments.

439 While the reduction in Γ (Figure 1) of $\sim 30\%$ at 50 hPa is significant, it is neither
 440 clear if this change is representative of other altitudes within the stratosphere nor how
 441 this age bias imprints on real chemical species. To this end, we begin by comparing the
 442 full latitude-pressure distribution of changes in Γ and another passive tracer (e90) (Fig-
 443 ure 4) between the CCMI Phase 1 and Phase 2 model configurations (red and green lines,
 444 Figure 1). In particular, we find that the changes in both passive tracers – large reduc-
 445 tions in Γ within both hemispheres (Fig. 4, top right) and increased values of e90 within
 446 the lower stratosphere (Fig. 4, bottom right) – are reflective of an overall increase in the
 447 strength of the transport circulation. This is highlighted in the CCMI Phase 2 – 1 model
 448 differences for the passive tracer distributions (Fig. 4, right panels) which are shown in
 449 the absence of robust observational constraints of Γ at higher altitudes (or any obser-
 450 vational constraints for e90, for that matter). The reduced/increased stratospheric bur-
 451 dens of the age and e90 tracers are consistent with stronger upwelling in the CCMI Phase
 452 2 model configuration (Figure 2).

453 While the observational constraints on Γ presented in Figure 1 and the departure
 454 of w^* away from MERRA-2 suggest that transport properties of the newer model con-
 455 figurations are moving in the wrong direction, it is relevant to ask whether or not the
 456 trace gas satellite measurements also support this conclusion. Indeed, comparisons with
 457 observations show larger biases in N_2O (Fig. 5, top panels) and CH_4 (Fig. 5, bottom pan-
 458 els), increasing from 10% to 30% in the CCMI Phase 2 model configuration, depending
 459 on the species. The patterns of these biases are generally consistent with the biases in
 460 the mean age (Fig. 4), suggesting a strong link between the tracers. Recall that the same
 461 chemistry mechanism is used in both CCMI Phase 1 and 2 simulations.

462 The fact that the mean age changes have a significant imprint on the simulated trace
 463 gases is consequential for the GEOS-R21C system. However, the configurations shown
 464 in Fig. 1-5 differ in many respects (physics, resolution, radiation, FV remapping algo-
 465 rithm) and it is difficult to meaningfully interpret what is driving the changes in w^* (and
 466 the tracers). We therefore move next to the targeted model experiments (Table 2) in or-

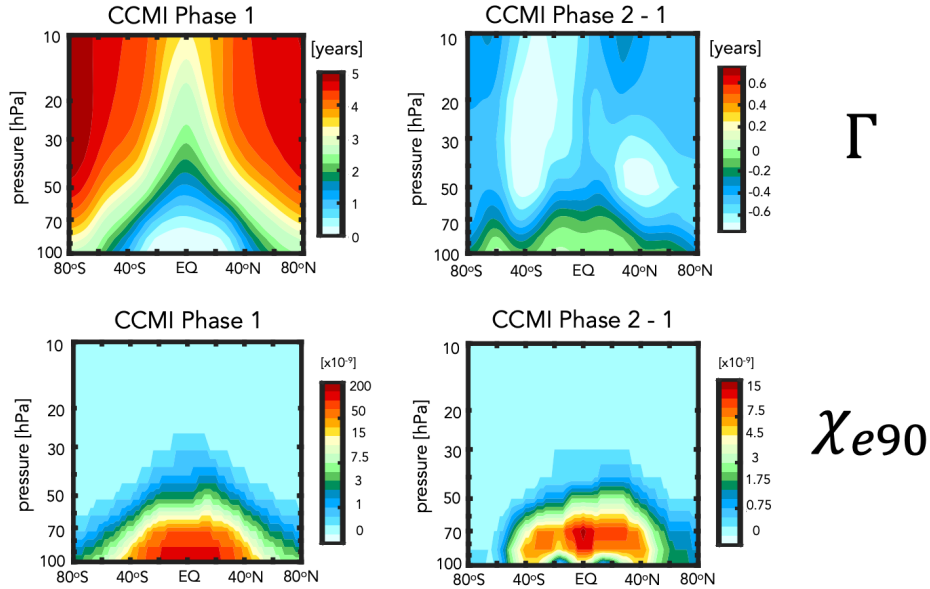


Figure 4. The climatological mean (2000-2010) distribution of the mean age-of-air (Γ) (left, top) and e90 idealized tracers (left, bottom) for the CCMI Phase 1 model configuration. Climatological differences between the CCMI Phase 2 and Phase 1 model configurations are shown in the right panels. Note that a nonlinear colorbar has been used in the e90 subplots.

467 der to interpret the model development steps that resulted in these transport circula-
 468 tion changes.

469 **3.2 Identifying Drivers of Upwelling and Tracer Changes Since** 470 **MERRA-2**

471 *3.2.1 Radiation versus REMAP Algorithm*

472 As discussed in Section 2, among the model changes that were made since MERRA-
 473 2, the changes in radiation and the FV remapping algorithm are most likely to directly
 474 have impacted the stratospheric circulation. We therefore begin by assessing which of
 475 these changes dominates the decreases in Γ shown in Figure 1.

476 Figure 6 shows the distribution of Γ for experiments in which the longwave, short-
 477 wave, and REMAP updates since MERRA-2 have successively been undone. Relative
 478 to the control experiment (CTRL; Table 2, row 1), the reversion back to Chou and Suarez
 479 (1994) in the shortwave and Chou (1990, 1992) in the longwave results in an increase in
 480 the mean age of ~ 0.5 years throughout the stratosphere (CSRAD; Table 2, row 2). Though
 481 significant, this change in Γ is smaller than the change that results from reverting back
 482 to REMAP Option 1 (M2REMAP; Table 1; row 3), in which the mean age increases by
 483 ~ 1 year. The combined impacts of both changes (CSRAD+M2REMAP; Table 1 row
 484 4) is roughly linear, with age values of ~ 5.5 years over high latitudes at 50 hPa, con-
 485 sistent with the values simulated by the GEOS-CTM MERRA-2 integration (black line,
 486 Figure 1) and with the CCMI Phase-1 version of the model (red line, Figure 1).

487 Next we ask if the behavior of Γ exhibited in Figure 6 can be interpreted in terms
 488 of changes in the strength of lower stratospheric tropical upwelling and extratropical wave

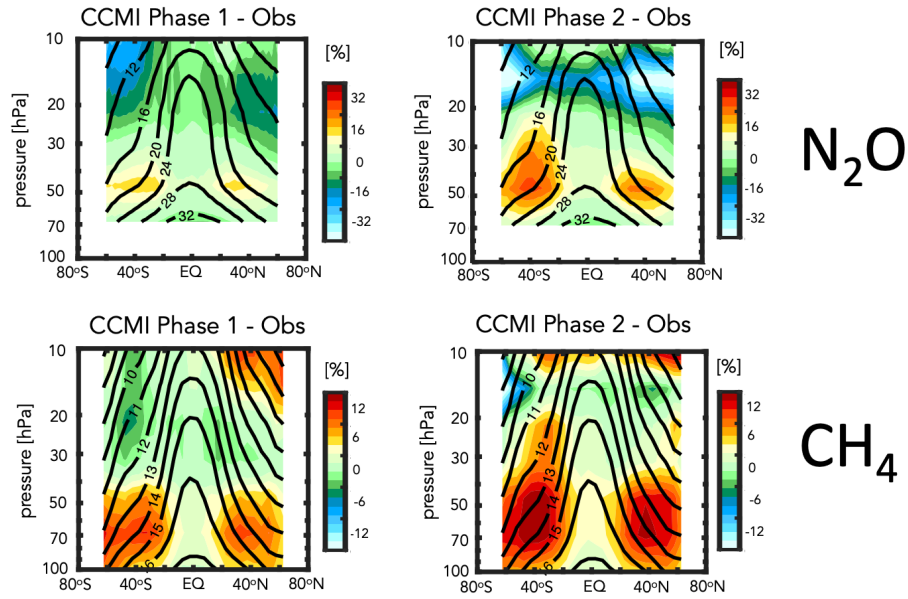


Figure 5. Colors shown anomalies in the simulated distributions of nitrous oxide (N_2O) (top) and methane (CH_4) (bottom), relative to the MLS and HALOE observed values, respectively, for the CCMI Phase 1 (left) and Phase 2 (right) GEOS model configurations. Climatological mean observed values are shown in the black contours.

Annual Climatological Mean Stratospheric Mean Age (Γ)

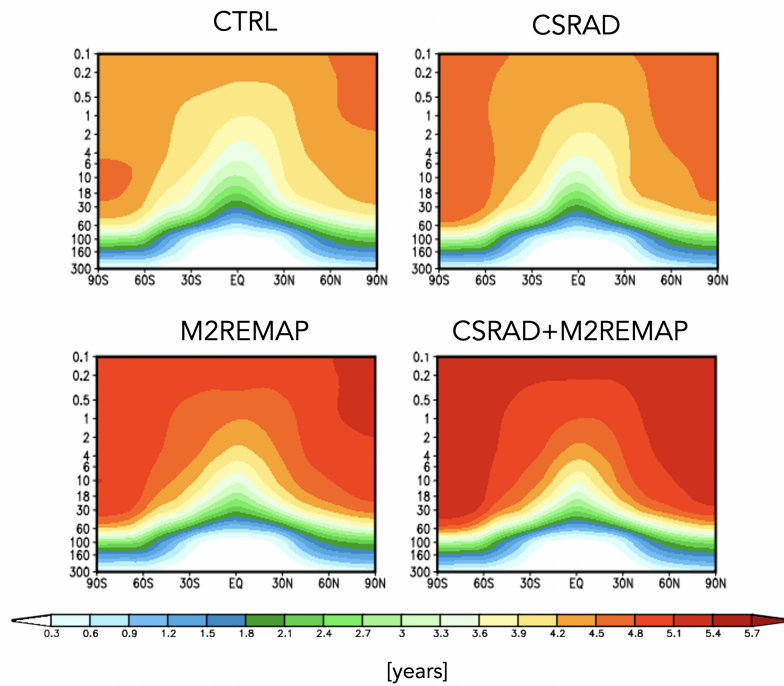


Figure 6. Colors show the simulated 2000-2010 climatological annual mean distributions of the mean age-of-air (Γ) for the CTRL (top left; Table 1, row 1), CSRAD (top right; Table 1, row 2), M2REMAP (bottom left; Table 1, row 3) and combined CSRAD+M2REMAP (bottom right; Table 1, row 4) experiments.

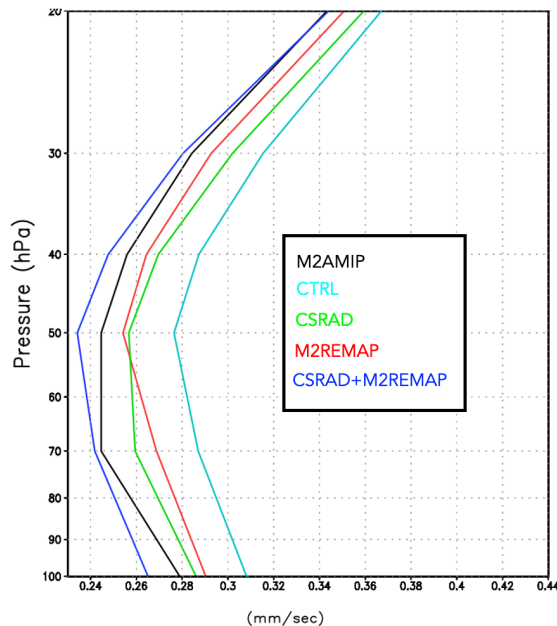
DJF Climatological Mean Tropical Upwelling (w^*)

Figure 7. The DJF 1985-2015 climatological mean vertical residual mean velocity, w^* , averaged between the turnaround latitudes for the CTRL (cyan line; Table 2, row 1), CSRAD (green line; Table 2, row 2), M2REMAP (red line; Table 2, row 3) and combined CSRAD+M2REMAP (blue line; Table 2, row 4) experiments. M2AMIP is shown in black.

489 convergence, as our previous analysis of the CCM1 experiments suggested. Indeed, Fig-
 490 ure 7 shows that values of upwelling decrease in the CSRAD and M2REMAP experiments,
 491 relative to the CTRL integration. The increase in upwelling resulting from both changes
 492 (CSRAD+M2REMAP) is still larger, consistent with the larger age decreases in that ex-
 493 periment. This change in the behavior of w^* within the tropical stratosphere can be in-
 494 terpreted in terms of changes in the Eliassen Palm flux convergence over NH midlati-
 495 tudes (not shown), which features smaller values in the CSRAD, M2REMAP (and CSRAD+
 496 MSREMAP) experiments. Note that our examination of the changes in w^* are derived
 497 from EMIP integrations, which we showed previously converge (for DJF) to the statis-
 498 tics derived from corresponding AMIP experiments.

499 3.2.2 FV REMAP Algorithm: Sensitivity of Climate Statistics

500 Having shown in the previous section that the largest changes in the mean age were
 501 realized through the reversion back to REMAP Option 1, we now investigate further the
 502 sensitivity of the transport circulation to the choice of remapping interpolation scheme.
 503 In particular, we compare simulations in which total energy is calculated at new mid-
 504 layer pressures using cubic, quadratic and linear interpolation prior to the aposterior in-
 505 tegral conservation (Table 2, rows 5-7). In addition, in this section we seek to understand
 506 how the changes in the Eliassen-Palm flux convergence over NH midlatitudes arise via
 507 analysis of the large-scale wind structure.

508 Figure 8 (left panel) shows a clear sensitivity in tropical upwelling to the choice of
 509 interpolation scheme, with w^* progressively increasing in strength moving from the CU-
 510 BIC to QUADRATIC to LINEAR schemes. This sensitivity is robust across horizontal

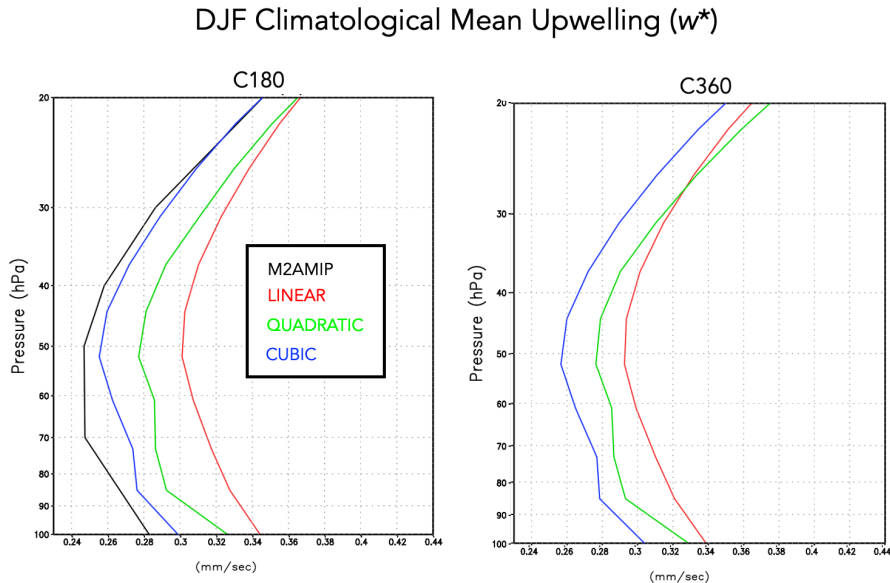


Figure 8. The DJF 1985-2015 climatological mean vertical residual mean velocity, w^* , averaged between the turnaround latitudes for the LINEAR (red line; Table 2, row 5), QUADRATIC (green line; Table 2, row 6) and CUBIC (blue line; Table 2, row 7) experiments. M2AMIP is shown in black. Results from C180 and C360 EMIP experiments are shown in the left and right panels, respectively.

511 resolutions as the same suite of experiments performed at C360 exhibit the same sensi-
 512 tivity (Fig. 8, right panel). While no current model version actually employs a linear
 513 scheme, this suite of experiments highlights the strong sensitivity to choice of interpo-
 514 lation scheme within the remapping algorithm; to the best of our knowledge, this result
 515 has not been reported in the literature. Furthermore, as we show next, this clean set of
 516 experiments allow us to inquire mechanistically into the processes that are driving the
 517 changes in wave convergence over midlatitudes, unencumbered by differences in horizon-
 518 tal resolution, physics, etc.

519 Consistent with our expectations based on the analysis of the previous experiments,
 520 the drivers of the changes in w^* are related to increased wave convergence moving from
 521 the CUBIC to QUADRATIC to LINEAR schemes (Figure 9). Over extratropical lati-
 522 tudes, the zonal force associated with this enhanced wave convergence is associated with
 523 enhanced downwelling at high latitudes that, through mass balance, is accompanied by
 524 enhanced upwelling in the tropics. This indirect impact of higher latitude wave drag is
 525 evident in Appendix Figure C1, which shows stronger upwelling/downwelling in the LIN-
 526 EAR and QUADRATIC experiments over the tropics/polar region.

527 Next we exploit the fact that these experiments only differ with respect to the in-
 528 terpolation scheme in order to inquire further into the drivers of the wave convergence
 529 changes. To this end, Figure 10 compares profiles of the zonal mean zonal wind between
 530 the CUBIC, QUADRATIC and LINEAR experiments, averaged over the region of en-
 531 hanced wave convergence (i.e. 20°N-60°N). The experiments featuring stronger wave con-
 532 vergence (LINEAR and QUADRATIC) are also simulations with stronger zonal winds,
 533 relative to MERRA-2, especially above 70 hPa. This change in winds occurs at both C180
 534 (Fig. 10, left panel) and C360 (Fig. 10, right panel) resolutions.

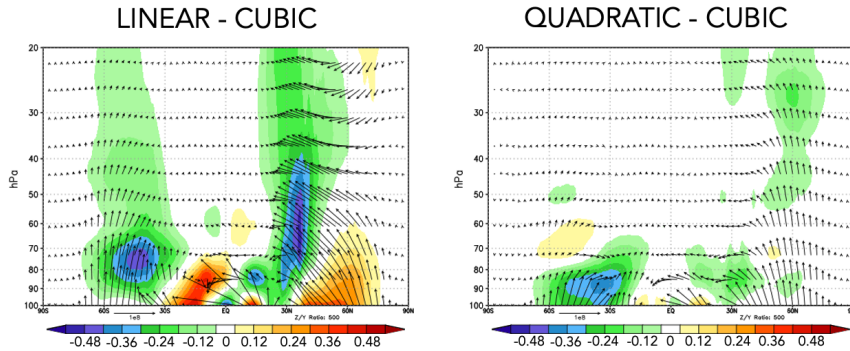
DJF Climatological Mean Eliassen-Palm Flux Divergence ($\nabla \cdot \mathbf{F}$)

Figure 9. Colors shown anomalies in the DJF 1985-2015 climatological mean Eliassen-Palm (EP) flux divergence in the LINEAR (left) and QUADRATIC (right) experiments, relative to the CUBIC model experiment. Arrows denote anomalies in the vertical and meridional EP flux vectors.

535 Structurally, the increase in zonal wind strength over northern extratropical mid-
 536 latitudes is reflective of a poleward shift in the zonal winds as the critical latitude, i.e.
 537 where the zonal wind is zero, shifts northward in the QUADRATIC and, especially, LIN-
 538 EAR integrations, relative to the CUBIC experiment (Figure 11). Since stationary waves
 539 only propagate in westerly zonal flow, the latitude where zonal flow is zero acts a bound-
 540 ary for wave propagation (Hardiman et al. (2014)). As a result, this shift in critical lat-
 541 itude results in enhanced wave propagation and convergence over middle and high lat-
 542 itudes.

543 Figures 10 and 11 highlight how the changes in zonal winds in the LINEAR and
 544 QUADRATIC experiments reflect a degradation in model skill, relative to MERRA-2,
 545 throughout the entire stratosphere. The changes in upwelling, mean age, chemical trace
 546 gases and zonal winds thus provide a coherent and self-consistent picture suggestive of
 547 a degradation in the representation of the stratospheric circulation since MERRA-2. That
 548 is, an increased bias in the stratospheric northern zonal winds are, via their influence on
 549 wave convergence, compromising changes in the strength of the mean meridional over-
 550 turning circulation and its impact on composition. It is interesting to note that the wind
 551 biases also extend into the troposphere and show degraded skill relative to MERRA-2
 552 in the LINEAR and QUADRATIC experiments (Figure 11). Examination of other fields
 553 (i.e. tropopause biases, Appendix Figure D1) present somewhat more of a nuanced story
 554 that depends more sensitively on latitude and season considered. The improvements in
 555 the zonal winds, however, are most relevant for setting the upwelling characteristics within
 556 the tropical lower stratosphere via their influence on wave propagation into that region.

557 Finally, to better understand why these impacts on the winds have such a conse-
 558 quence for the wave convergence properties within the stratosphere, next we examine the
 559 zonal structure of these biases in the middle stratosphere (Figure 12). This reveals that
 560 the enhanced winds in the LINEAR (and, to a lesser extent, QUADRATIC) integrations
 561 are concentrated over the North Pacific at both C180 (Fig. 12, left) and C360 (Fig. 12,
 562 right) resolutions (a similar picture emerges within the troposphere, not shown). As this
 563 region is the primary region dominating the stationary component of the upward flux
 564 of vertical wave activity (Plumb (1985), see their Figure 4) it is perhaps not surprising

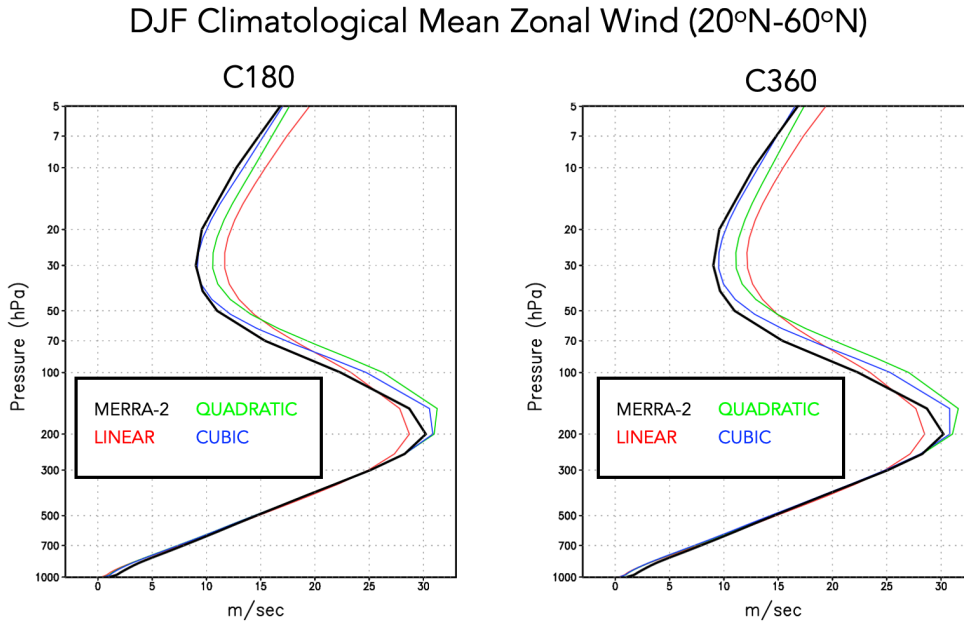


Figure 10. Vertical profiles of the DJF 1985-2015 climatological mean zonal mean zonal winds in the LINEAR (red), QUADRATIC (green) and CUBIC (blue) experiments, averaged between 20°N and 60°N. MERRA-2 is shown in the black line. Results for both C180 (left) and C360 (right) experiments are shown.

565 that this region is having a profound impact on the mean overturning circulation. Again,
 566 as with the zonal mean wind changes, the increases in wind strength over the North Pa-
 567 cific represent degraded model skill relative to MERRA-2. Note that comparisons with
 568 ERA-5 reveal a similar bias (not shown).

569 4 Conclusions

570 Here we have performed an analysis aimed at understanding differences in the rep-
 571 resentation of the stratospheric circulation in recent candidate systems for GEOS-R21C,
 572 relative to older versions of GEOS similar to the model used to produce MERRA-2. Us-
 573 ing targeted experiments oriented at disentangling various model development updates,
 574 we have identified a key role played by changes in the remapping algorithm within the
 575 model's finite-volume dynamical core. Our key results are as follows:

576 #1. The stratospheric mean age-of-air in GEOS is sensitive to the degree of the
 577 interpolation scheme that is used to calculate layer-mean values of total energy, U, V and
 578 tracers. Different treatment of the vertical remapping algorithm (REMAP Option 1 vs.
 579 2) result in mid-stratospheric (50 hPa) age-of-air differences of ~ 1 year over high lat-
 580 itudes, or about 30% climatological mean values.

581 #2. The age-of-air sensitivities reflect, to first order, changes in the strength of tropi-
 582 cal upwelling associated with the Brewer-Dobson circulation which are in turn driven
 583 by changes in EP flux convergence over northern midlatitudes. Changes in wave conver-
 584 gence reflect shifts in (critical lines of) wave propagation that originate in the troposphere
 585 over the Pacific Ocean, a region of strong upward wave activity.

DJF Climatological Zonal Mean Zonal Wind Anomalies Relative to MERRA-2

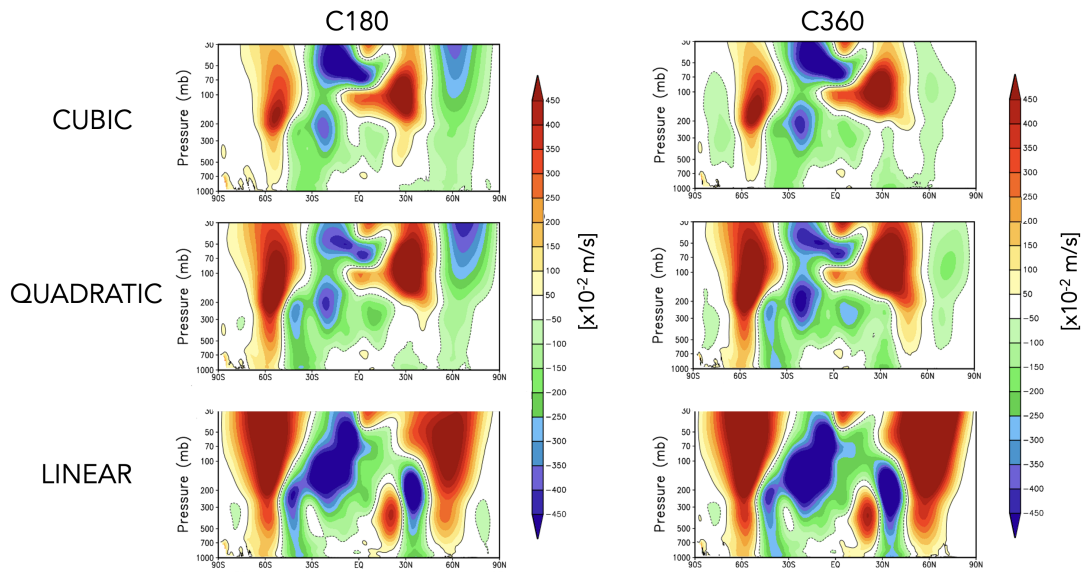


Figure 11. Colors shown anomalies in the DJF 1985-2015 climatological mean zonal mean zonal winds in the CUBIC (top), QUADRATIC (middle) and LINEAR (bottom) experiments, relative to MERRA-2. Results for both C180 (left) and C360 (right) experiments are shown.

DJF Climatological 30 hPa Zonal Wind Anomalies Relative to MERRA-2

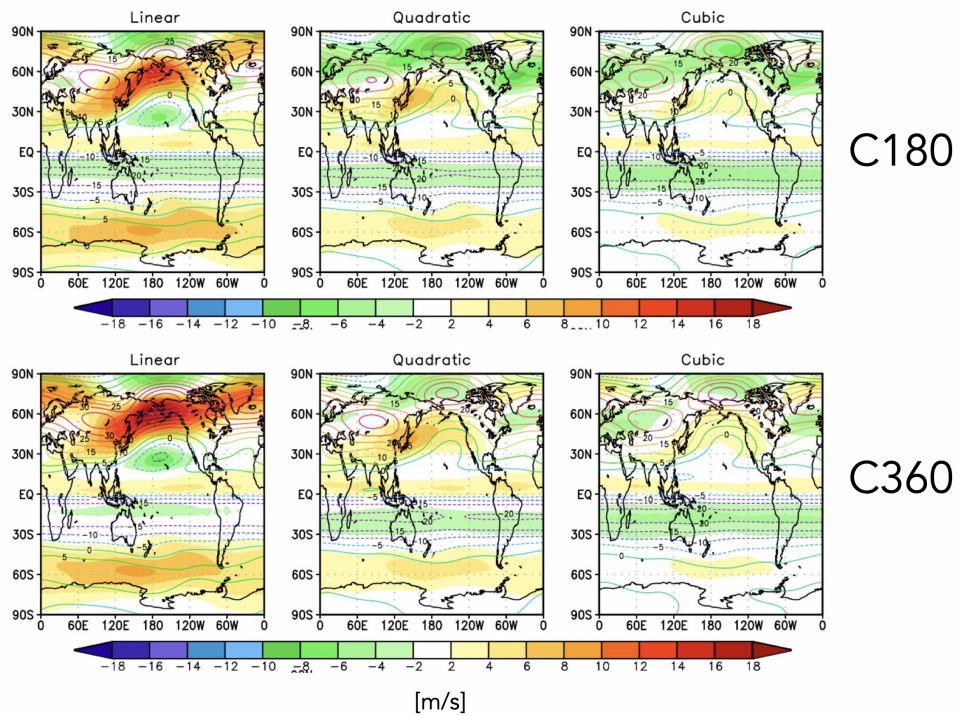


Figure 12. Colors shown anomalies in the DJF 1985-2015 climatological mean zonal winds at 30 hPa in the CUBIC (right), QUADRATIC (middle) and LINEAR (left) experiments, relative to MERRA-2. Results for both C180 (top) and C360 (bottom) experiments are shown.

586 #3. The degradation of upwelling statistics manifest in AMIPs, also translate to
 587 degradations in DAS configurations of GEOS.

588 Although our focus here has been on the stratospheric transport circulation, mo-
 589 tivating our use of tracer-independent metrics like the age-of-air, our results have clear
 590 implications for constituent transport in the next reanalysis that is currently under de-
 591 velopment (GEOS-R21C). In particular, we showed that the increased age-of-air biases
 592 correspond to increased biases in the representations of CH₄ and N₂O moving from the
 593 CCM1 Phase 1 to Phase 2 model configuration. This comports with well-known corre-
 594 lations between the mean age and stratospheric trace gases, reinforcing the fact that model
 595 transport inaccuracies continue to significantly affect simulations of important long-lived
 596 chemical species in the stratosphere (Hall et al. (1999)).

597 Our results highlight the key role played by model numerics in transport (e.g., Rood
 598 (1987)). The sensitivities in the age-of-air documented herein are also consistent in spirit
 599 with the findings in Gupta et al. (2020) who showed significant age differences occurring
 600 between spectral versus finite-volume numerics. Our results, however, suggest that there
 601 remain large sensitivities even within a given (FV) dynamical core. Furthermore, we also
 602 briefly show that that statistics derived from long AMIPS also manifest within a data
 603 assimilation context, which raises important questions as to the degree to which model
 604 biases can be ameliorated through assimilation of observations.

605 Looking forward, our findings support and build on the recommendation proposed
 606 in Gupta et al. (2020) for the construction of dynamical core benchmark tests aimed at
 607 determining how underlying AGCM numerics impact climatological transport proper-
 608 ties. In particular, in addition to the age-of-air, the authors propose a range of strato-
 609 spheric circulation diagnostics that should be evaluated including the zonal mean zonal
 610 winds, eddy temperature variance and zonal spectra of eddy kinetic energy. Our anal-
 611 ysis reveals an important role to be played by the climatological zonal mean wind struc-
 612 ture as it impacts wave convergence over midlatitudes; we therefore also recommend ex-
 613 plicit consideration of the Eliassen Palm flux convergence and tropical upwelling (w^*)
 614 fields as they may be crucial for interpreting age-of-air changes.

615 One somewhat incidental – but practical - result from our analysis is that the statis-
 616 tics of $\nabla \cdot F$ and w^* are well approximated by ensembles of so-called EMIP integrations.
 617 As these are substantially easier to run than AMIPs these could provide a “first pass”
 618 when evaluating new proposed model development changes, without the immediate need
 619 to integrate AMIP-style experiments. We emphasize, however, that this statement should
 620 only apply to a first stage in model development as the age-of-air will reflect the time
 621 integrated impacts of both advection and mixing.

622 Finally, we conclude by noting that, while we have focused on sensitivities within
 623 the FV remapping algorithm, our results have highlighted important sensitivities to changes
 624 in radiation and, to a lesser extent, changes in parameterized convection. Though not
 625 the dominant drivers of the age-of-air changes identified here, the former could poten-
 626 tially influence the age both directly through changes in thermal structure and indirectly
 627 by modifying wave propagation and/or generation in the troposphere. Future work will
 628 focus on examining these impacts.

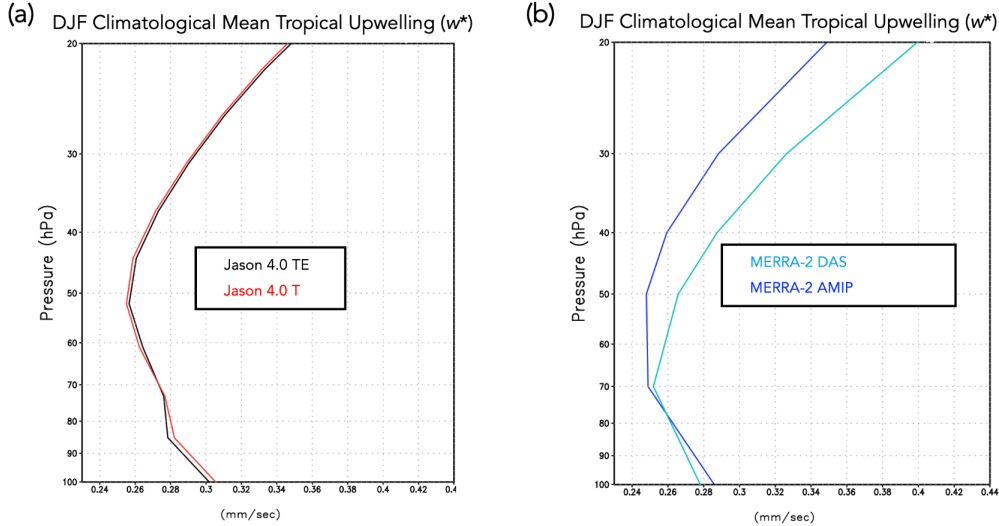


Figure A1. The DJF 1985-2015 climatological mean vertical residual mean velocity, w^* , averaged between the turnaround latitudes compared between two Jason 4.0 experiments remapping to temperature (T) (red) versus total energy (TE) (black) (a) and between MERRA-2 DAS (cyan) and the M2AMIP ensemble (blue) (b).

629

Appendix A Sensitivities in Calculation of TEM Upwelling

630

631

632

633

634

635

636

637

638

639

640

There are various aspects of the calculation of the TEM circulation that warrant further comment. First, whereas the modeling experiments listed in Table 2 (rows 5-7) focus on the sensitivity of Step 5 in REMAP Option 1 to the choice of interpolation scheme, another difference between REMAP Options 1 and 2 is the use of TE versus T, respectively. To test the impact of this difference, we ran a new experiment which is identical to the CUBIC experiment (Table 2, row 7), except that T is remapped from input layer mean pressure locations to standard output layer mean locations directly using cubic interpolation (i.e., no computation of TE or a-posteriori energy conservation applied). Appendix Figure A1a shows that this has little impact on the strength of tropical upwelling, suggesting that the w^* differences between REMAP Options 1 and 2 are dominated by sensitivities to the choice of interpolation scheme, not the use of TE versus T.

641

642

643

644

645

646

647

Second, the vertical component of the TEM circulation (w^*) shows some differences in vertical structure between MERRA-2 and the 30-member M2AMIP ensemble (Appendix Figure A1b). This difference in vertical structure appears to reflect a difference between DAS and free-running configurations of the model, since both DAS configurations shown in Figure 2b share a similar vertical structure. Given this difference, we ensure as apples-to-apples a comparison of simulated TEM velocities by comparing all AMIP results to other AMIPS, and vice versa for the few selected DAS results.

648

Appendix B Correspondence between EMIP and AMIP Upwelling

649

650

651

652

Appendix Figure B1 shows the close correspondence in DJF climatological mean w^* , averaged between the turnaround latitudes, from AMIP and EMIP experiments using the same model configuration. This good agreement in upwelling is used to justify the analysis of the EMIP experiments listed in Table 2 (rows 5-7).

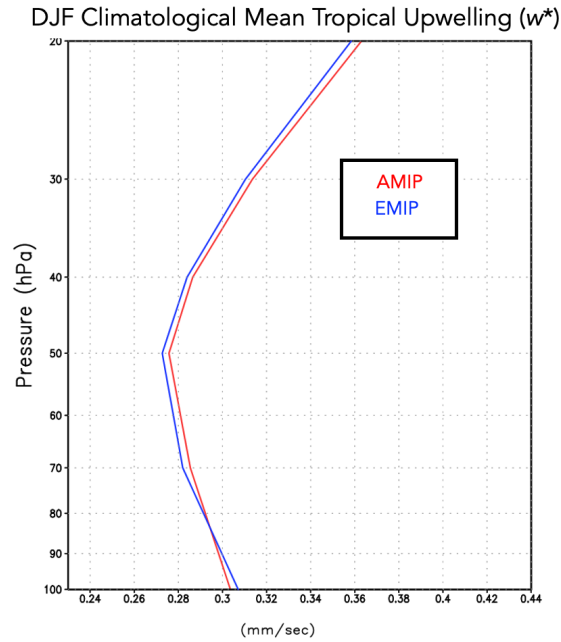


Figure B1. The DJF 1985-2015 climatological mean vertical residual mean velocity, w^* , averaged between the turnaround latitudes for the CTRL experiment (Table 2, row 1). Results based on a 30-year-long AMIP experiment (red line) and a 30-member ensemble of three-month-long EMIP experiments (blue line) are shown.

653 **Appendix C Changes in Tropical and High Latitude Upwelling**

654 Appendix Figure C1 compares the behavior in residual mean upwelling among the
 655 LINEAR, QUADRATIC and CUBIC experiments over the latitudes between the (tropi-
 656 cal) turnaround latitudes (left) and poleward of the northern turnaround latitude (right).
 657 The ordering among experiments in both regions reflects how increases in downwelling
 658 at high latitudes are, through mass balance, accompanied by enhanced upwelling in the
 659 tropics.

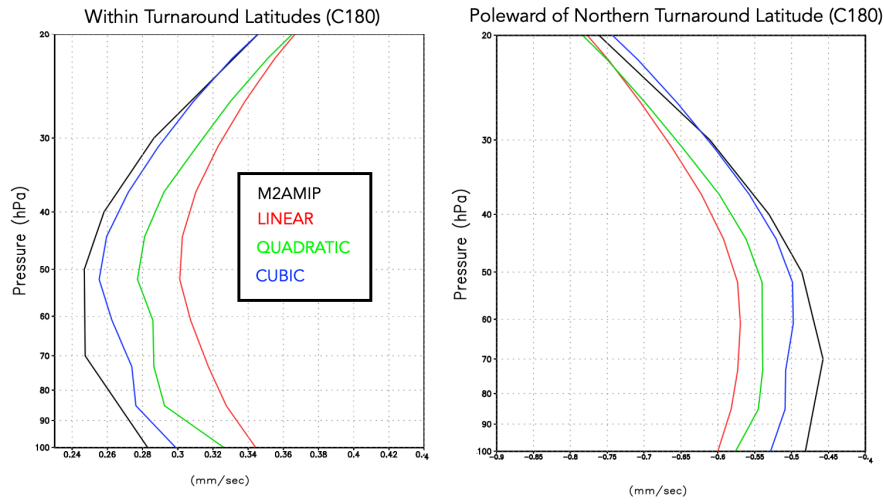
DJF Climatological Mean Upwelling (w^*)

Figure C1. Left: The DJF 1985–2015 climatological mean vertical residual mean velocity, w^* , averaged between the turnaround latitudes for the LINEAR (red line; Table 2, row 5), QUADRATIC (green line; Table 2, row 6) and CUBIC (blue line; Table 2, row 7) experiments. M2AMIP is shown in black. Right: As in left panel, except averaged over latitudes poleward of the northern turnaround latitude. Results in both panels are shown for C180 experiments.

660

Appendix D Tropopause Pressure

661

Appendix Figure D1 compares boreal winter tropopause pressure and temperature among the LINEAR, QUADRATIC and CUBIC experiments, relative to MERRA-2.

662

DJF Climatological Mean Tropopause

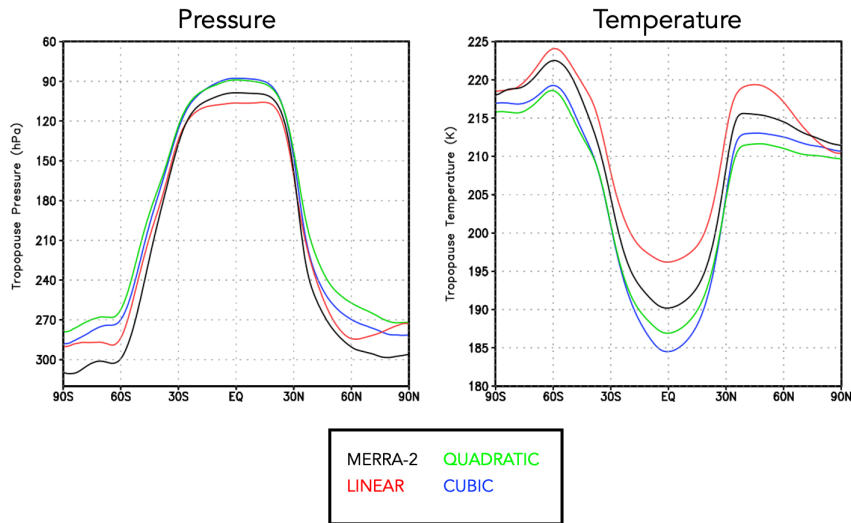


Figure D1. The DJF 1985-2015 climatological mean tropopause pressure (left) and temperature (right) in the CUBIC (blue), QUADRATIC (green) and LINEAR (red) experiments. MERRA-2 is shown in black. Results are shown for the C180 experiments.

663 Acronyms

- 664 **AMIP** Atmospheric Model Intercomparison Project
 665 **CH₄** methane
 666 **CCMs** chemistry climate models
 667 **CCMI** Chemistry Climate Modeling Initiative
 668 **CCMVal** Chemistry Climate Model Validation
 669 **CO₂** carbon dioxide
 670 **CTRL** control
 671 **CTM** chemistry transport model
 672 **DAS** Data assimilation
 673 **DJF** December-January-February
 674 **EMIP** ensemble AMIP
 675 **EOS** Earth Observing System
 676 **EP** Eliassen-Palm
 677 **FV** finite volume
 678 **GEOS** Global Earth Observing System
 679 **GEOS-R21C** GEOS Retrospective analysis for the 21st Century
 680 **GMI** Global Modeling Initiative
 681 **HALOE** Halogen Occultation Experiment
 682 **MERRA-2** Modern-Era Retrospective Analysis for Research and Applications v2
 683 **MLS** Microwave Limb Sounder
 684 **N₂O** nitrous oxide
 685 **NH** northern hemisphere
 686 **PPM** piecewise parabolic
 687 **RRTMG** Rapid Radiative Transfer Model for GCMs
 688 **SW** shortwave

689 **TE** total energy
 690 **TEM** Transformed Eulerian Mean
 691 **UARS** Upper Atmosphere Research Satellite

692 **Open Research Section**

693 TBD

694 **Acknowledgments**

695 C.O. thanks William Putnam and Lawrence Coy for their insight which helped in inter-
 696 preting the results and guiding experimental design. The authors also thank the high-
 697 performance computing resources provided by NASA’s Advanced Supercomputing (NAS)
 698 Division and the NASA Center for Climate Simulation (NCCS) as well as NASA’s Mod-
 699 eling, Analysis and Prediction (MAP) program, which supports the Global Modeling As-
 700 simulation Office and core chemistry-climate and chemistry-modeling activities.

701 **References**

- 702 Abalos, M., Calvo, N., Benito-Barca, S., Garny, H., Hardiman, S. C., Lin, P., ...
 703 others (2021). The Brewer–Dobson circulation in CMIP6. *Atmospheric*
 704 *Chemistry and Physics*, *21*(17), 13571–13591.
- 705 Abalos, M., Orbe, C., Kinnison, D. E., Plummer, D., Oman, L. D., Jöckel, P., ...
 706 others (2020). Future trends in stratosphere-to-troposphere transport in CCM1
 707 models. *Atmospheric Chemistry and Physics*, *20*(11), 6883–6901.
- 708 Abalos, M., Randel, W. J., Kinnison, D. E., & Garcia, R. R. (2017). Using the
 709 artificial tracer e90 to examine present and future UTLS tracer transport in
 710 WACCM. *Journal of the Atmospheric Sciences*, *74*(10), 3383–3403.
- 711 Andrews, D., Holton, J., & Leovy, C. (1987). Middle Atmosphere Dynam-
 712 ics. *Academic Press*, *60*, 489. doi: 10.1175/1520-0469(2003)060<0103:
 713 CEOOAL>2.0.CO;2
- 714 Arnold, N. P., Putman, W. M., & Freitas, S. R. (2020). Impact of resolution and
 715 parameterized convection on the diurnal cycle of precipitation in a global
 716 nonhydrostatic model. *Journal of the Meteorological Society of Japan. Ser. II*.
- 717 Boering, K. A., Wofsy, S., Daube, B., Schneider, H., Loewenstein, M., Podolske, J.,
 718 & Conway, T. (1996). Stratospheric mean ages and transport rates from obser-
 719 vations of carbon dioxide and nitrous oxide. *Science*, *274*(5291), 1340–1343.
- 720 Butchart, N., Cionni, I., Eyring, V., Shepherd, T., Waugh, D., Akiyoshi, H., ...
 721 others (2010). Chemistry–climate model simulations of twenty-first century
 722 stratospheric climate and circulation changes. *Journal of Climate*, *23*(20),
 723 5349–5374.
- 724 Chiodo, G., & Polvani, L. M. (2019). The response of the ozone layer to quadru-
 725 pled CO2 concentrations: Implications for climate. *Journal of Climate*, *32*(22),
 726 7629–7642.
- 727 Chou, M.-D. (1990). Parameterizations for the absorption of solar radiation by O2
 728 and CO2 with application to climate studies. *Journal of Climate*, *3*(2), 209–
 729 217.
- 730 Chou, M.-D. (1992). A solar radiation model for use in climate studies. *Journal of*
 731 *Atmospheric Sciences*, *49*(9), 762–772.
- 732 Chou, M.-D., & Suarez, M. J. (1994). An efficient thermal infrared radiation param-
 733 eterization for use in general circulation models.
- 734 Collow, A. B. M., Mahanama, S. P., Bosilovich, M. G., Koster, R. D., & Schubert,
 735 S. D. (2017). *An evaluation of teleconnections over the united states in an*
 736 *ensemble of AMIP simulations with the MERRA-2 configuration of the GEOS*

- 737 *atmospheric model* (Tech. Rep.).
- 738 Davis, N. A., Callaghan, P., Simpson, I. R., & Tilmes, S. (2022). Specified dynamics
739 scheme impacts on wave-mean flow dynamics, convection, and tracer transport
740 in CESM2 (WACCM6). *Atmospheric Chemistry and Physics*, *22*(1), 197–214.
- 741 Dietmüller, S., Eichinger, R., Garny, H., Birner, T., Boenisch, H., Pitari, G., . . .
742 others (2018). Quantifying the effect of mixing on the mean age of air in
743 CCMVal-2 and CCM1-1 models. *Atmospheric Chemistry and Physics*, *18*(9),
744 6699–6720.
- 745 Eichinger, R., Garny, H., Šácha, P., Danker, J., Dietmüller, S., & Oberländer-Hayn,
746 S. (2020). Effects of missing gravity waves on stratospheric dynamics: Part 1,
747 Climatology. *Climate Dynamics*, *54*(5), 3165–3183.
- 748 Eluszkiewicz, J., Hemler, R. S., Mahlman, J. D., Bruhwiler, L., & Takacs, L. L.
749 (2000). Sensitivity of age-of-air calculations to the choice of advection scheme.
750 *Journal of the Atmospheric Sciences*, *57*(19), 3185–3201.
- 751 Eyring, V., Lamarque, J.-F., Hess, P., Arfeuille, F., Bowman, K., Chipperfield,
752 M. P., . . . others (2013). Overview of IGAC/SPARC Chemistry-Climate
753 Model Initiative (CCMI) community simulations in support of upcoming ozone
754 and climate assessments. *SPARC Newsletter*, *40*(January), 48–66.
- 755 Freitas, S. R., Grell, G. A., Molod, A., Thompson, M. A., Putman, W. M., Santos e
756 Silva, C. M., & Souza, E. P. (2018). Assessing the Grell-Freitas convection
757 parameterization in the NASA GEOS modeling system. *Journal of Advances
758 in Modeling Earth Systems*, *10*(6), 1266–1289.
- 759 Freitas, S. R., Putman, W. M., Arnold, N. P., Adams, D. K., & Grell, G. A. (2020).
760 Cascading toward a kilometer-scale GCM: Impacts of a scale-aware convection
761 parameterization in the Goddard Earth Observing System GCM. *Geophysical
762 Research Letters*, *47*(17), e2020GL087682.
- 763 Fujiwara, M., Manney, G. L., Gray, L. J., Wright, J. S., Tegtmeier, S., Ivanciu, I., &
764 Pilch Kedzierski, R. (2022). Sparc reanalysis intercomparison project (s-rip)
765 final report.
- 766 Gelaro, R., McCarty, W., Suárez, M. J., Todling, R., Molod, A., Takacs, L., . . .
767 others (2017). The modern-era retrospective analysis for research and applica-
768 tions, version 2 (MERRA-2). *Journal of Climate*, *30*(14), 5419–5454.
- 769 Grell, G. A., & Freitas, S. R. (2014). A scale and aerosol aware stochastic convective
770 parameterization for weather and air quality modeling. *Atmospheric Chemistry
771 and Physics*, *14*(10), 5233–5250.
- 772 Grooß, J.-U., & Russell III, J. M. (2005). A stratospheric climatology for O₃, H₂O,
773 CH₄, NO_x, HCl and HF derived from HALOE measurements. *Atmospheric
774 Chemistry and Physics*, *5*(10), 2797–2807.
- 775 Gupta, A., Gerber, E. P., & Lauritzen, P. H. (2020). Numerical impacts on tracer
776 transport: A proposed intercomparison test of Atmospheric General Circula-
777 tion Models. *Quarterly Journal of the Royal Meteorological Society*, *146*(733),
778 3937–3964.
- 779 Hall, T. M., & Plumb, R. A. (1994). Age as a diagnostic of stratospheric transport.
780 *Journal of Geophysical Research: Atmospheres*, *99*(D1), 1059–1070.
- 781 Hall, T. M., Waugh, D. W., Boering, K. A., & Plumb, R. A. (1999). Evaluation
782 of transport in stratospheric models. *Journal of Geophysical Research: Atmo-
783 spheres*, *104*(D15), 18815–18839.
- 784 Hardiman, S. C., Butchart, N., & Calvo, N. (2014). The morphology of the Brewer-
785 Dobson circulation and its response to climate change in CMIP5 simulations.
786 *Quarterly Journal of the Royal Meteorological Society*, *140*(683), 1958–1965.
- 787 Haynes, P., McIntyre, M., Shepherd, T., Marks, C., & Shine, K. P. (1991). On the
788 “downward control” of extratropical diabatic circulations by eddy-induced
789 mean zonal forces. *Journal of the Atmospheric Sciences*, *48*(4), 651–678.
- 790 Hegglin, M. I., Brunner, D., Peter, T., Hoor, P., Fischer, H., Staehelin, J., . . . Weers,
791 U. (2006). Measurements of NO, NO_y, N₂O, and O₃ during SPURT: implica-

- 792 tions for transport and chemistry in the lowermost stratosphere. *Atmospheric*
793 *Chemistry and Physics*, 6(5), 1331–1350.
- 794 Holton, J. R., Haynes, P. H., McIntyre, M. E., Douglass, A. R., Rood, R. B., & Pfis-
795 ter, L. (1995). Stratosphere-troposphere exchange. *Reviews of Geophysics*,
796 33(4), 403–439.
- 797 Holzer, M., & Hall, T. M. (2000). Transit-time and tracer-age distributions in geo-
798 physical flows. *Journal of the atmospheric sciences*, 57(21), 3539–3558.
- 799 Iacono, M. J., Delamere, J. S., Mlawer, E. J., Shephard, M. W., Clough, S. A., &
800 Collins, W. D. (2008). Radiative forcing by long-lived greenhouse gases: Cal-
801 culations with the AER radiative transfer models. *Journal of Geophysical*
802 *Research: Atmospheres*, 113(D13).
- 803 Ivy, D. J., Solomon, S., Calvo, N., & Thompson, D. W. (2017). Observed connec-
804 tions of arctic stratospheric ozone extremes to Northern Hemisphere surface
805 climate. *Environmental Research Letters*, 12(2), 024004.
- 806 Kouatchou, J., Molod, A., Nielsen, J., Auer, B., Putman, W., & Clune, T. (2015).
807 *GEOS-5 chemistry transport model user’s guide* (Tech. Rep.).
- 808 Legras, B., Pissot, I., Berthet, G., & Lefèvre, F. (2004). Variability of the lagrangian
809 turbulent diffusivity in the lower stratosphere. *Atmospheric Chemistry and*
810 *Physics Discussions*, 4(6), 8285–8325.
- 811 Lin, S.-J. (2004). A “vertically lagrangian” finite-volume dynamical core for global
812 models. *Monthly Weather Review*, 132(10), 2293–2307.
- 813 Molod, A., Takacs, L., Suarez, M., & Bacmeister, J. (2015). Development of the
814 GEOS-5 atmospheric general circulation model: Evolution from MERRA to
815 MERRA2. *Geoscientific Model Development*, 8(5), 1339–1356.
- 816 Monge-Sanz, B., Chipperfield, M., Simmons, A., & Uppala, S. (2007). Mean age of
817 air and transport in a CTM: Comparison of different ECMWF analyses. *Geo-*
818 *physical Research Letters*, 34(4).
- 819 Monge-Sanz, B. M., Bozzo, A., Byrne, N., Chipperfield, M. P., Diamantakis, M.,
820 Flemming, J., ... others (2022). A stratospheric prognostic ozone for seam-
821 less Earth system models: performance, impacts and future. *Atmospheric*
822 *Chemistry and Physics*, 22(7), 4277–4302.
- 823 Morgenstern, O., & Carver, G. D. (2001). Comparison of cross-tropopause transport
824 and ozone in the upper troposphere and lower stratosphere region. *Journal of*
825 *Geophysical Research: Atmospheres*, 106(D10), 10205–10221.
- 826 Neu, J., Strahan, S., Braesicke, P., Douglass, A., Huck, P., Oman, L., ... Tegtmeier,
827 S. (2010). SPARC CCMVal (2010), SPARC Report on the Evaluation of
828 Chemistry-Climate Models: Chapter 5: Transport. SPARC.
- 829 Neu, J. L., & Plumb, R. A. (1999). Age of air in a “leaky pipe” model of strato-
830 spheric transport. *Journal of Geophysical Research: Atmospheres*, 104(D16),
831 19243–19255.
- 832 Oehrlein, J., Chiodo, G., & Polvani, L. M. (2020). The effect of interactive ozone
833 chemistry on weak and strong stratospheric polar vortex events. *Atmospheric*
834 *Chemistry and Physics*, 20(17), 10531–10544.
- 835 Orbe, C., Oman, L. D., Strahan, S. E., Waugh, D. W., Pawson, S., Takacs, L. L., &
836 Molod, A. M. (2017). Large-scale atmospheric transport in GEOS replay simu-
837 lations. *Journal of Advances in Modeling Earth Systems*, 9(7), 2545–2560.
- 838 Orbe, C., Rind, D., Jonas, J., Nazarenko, L., Faluvegi, G., Murray, L. T., ... oth-
839 ers (2020). GISS Model E2.2: A climate model optimized for the middle
840 atmosphere—2. Validation of large-scale transport and evaluation of cli-
841 mate response. *Journal of Geophysical Research: Atmospheres*, 125(24),
842 e2020JD033151.
- 843 Orbe, C., Yang, H., Waugh, D. W., Zeng, G., Morgenstern, O., Kinnison, D. E., ...
844 others (2018). Large-scale tropospheric transport in the Chemistry–Climate
845 Model Initiative (CCMI) simulations. *Atmospheric Chemistry and Physics*,
846 18(10), 7217–7235.

- 847 Pan, L. L., Wei, J., Kinnison, D., Garcia, R., Wuebbles, D., & Brasseur, G. P.
848 (2007). A set of diagnostics for evaluating chemistry-climate models in the ex-
849 tratropical tropopause region. *Journal of Geophysical Research: Atmospheres*,
850 *112*(D9).
- 851 Pawson, S., Stajner, I., Kawa, S. R., Hayashi, H., Tan, W.-W., Nielsen, J. E., ...
852 Livesey, N. J. (2007). Stratospheric transport using 6-h-averaged winds from
853 a data assimilation system. *Journal of Geophysical Research: Atmospheres*,
854 *112*(D23).
- 855 Plumb, R. A. (1985). On the three-dimensional propagation of stationary waves.
856 *Journal of Atmospheric Sciences*, *42*(3), 217–229.
- 857 Plumb, R. A. (1996). A “tropical pipe” model of stratospheric transport. *Journal of*
858 *Geophysical Research: Atmospheres*, *101*(D2), 3957–3972.
- 859 Plumb, R. A. (2002). Stratospheric transport. *Journal of the Meteorological Society*
860 *of Japan. Ser. II*, *80*(4B), 793–809.
- 861 Polvani, L. M., Waugh, D. W., Correa, G. J., & Son, S.-W. (2011). Stratospheric
862 ozone depletion: The main driver of twentieth-century atmospheric circulation
863 changes in the southern hemisphere. *Journal of Climate*, *24*(3), 795–812.
- 864 Prather, M. J., Zhu, X., Tang, Q., Hsu, J., & Neu, J. L. (2011). An atmospheric
865 chemist in search of the tropopause. *Journal of Geophysical Research: Atmo-*
866 *spheres*, *116*(D4).
- 867 Rood, R. B. (1987). Numerical advection algorithms and their role in atmospheric
868 transport and chemistry models. *Reviews of geophysics*, *25*(1), 71–100.
- 869 Rosenlof, K. H. (1995). Seasonal cycle of the residual mean meridional circulation
870 in the stratosphere. *Journal of Geophysical Research: Atmospheres*, *100*(D3),
871 5173–5191.
- 872 Son, S.-W., Tandon, N. F., Polvani, L. M., & Waugh, D. W. (2009). Ozone hole and
873 Southern Hemisphere climate change. *Geophysical Research Letters*, *36*(15).
- 874 Strahan, S., Douglass, A., & Newman, P. (2013). The contributions of chemistry
875 and transport to low arctic ozone in March 2011 derived from aura MLS obser-
876 vations. *Journal of Geophysical Research: Atmospheres*, *118*(3), 1563–1576.
- 877 Thiele, G., & Sarmiento, J. (1990). Tracer dating and ocean ventilation. *Journal of*
878 *Geophysical Research: Oceans*, *95*(C6), 9377–9391.
- 879 Waugh, D., & Hall, T. (2002). Age of stratospheric air: Theory, observations, and
880 models. *Reviews of Geophysics*, *40*(4), 1–1.
- 881 Weaver, C. J., Douglass, A. R., & Rood, R. B. (1993). Thermodynamic balance
882 of three-dimensional stratospheric winds derived from a data assimilation
883 procedure. *Journal of Atmospheric Sciences*, *50*(17), 2987–2993.